PHYSICAL REVIEW C **96**, 014310 (2017)

Nuclear deformation in the $A \approx 100$ region: Comparison between new masses and mean-field predictions

A. de Roubin,[1,2,*] D. Atanasov,[1,†] K. Blaum,[1] S. George,[1] F. Herfurth,[3] D. Kisler,[1] M. Kowalska,[4] S. Kreim,[1,4,‡] D. Lunney,[5] V. Manea,[1,§] E. Minaya Ramirez,[1,‖] M. Mougeot,[5] D. Neidherr,[3] M. Rosenbusch,[6,¶] L. Schweikhard,[6] A. Welker,[7,§] F. Wienholtz,[6,§] R. N. Wolf,[1,**] and K. Zuber[7]

[1]*Max-Planck-Institut für Kernphysik, Saupfercheckweg 1, D-69117 Heidelberg, Germany*

[2]*Centre d'Etudes Nucléaires de Bordeaux Gradignan, CNRS/IN2P3–Université de Bordeaux, F-33175 Gradignan Cedex, France*

[3]*GSI Helmholtzzentrum für Schwerionenforschung GmbH, D-64291 Darmstadt, Germany*

[4]*CERN, CH-1211 Geneva, Switzerland*

[5]*CSNSM-IN2P3-CNRS, Université Paris-Sud, F-91405 Orsay, France*

[6]*Ernst-Moritz-Arndt-Universität, Institut für Physik, D-17487 Greifswald, Germany*

[7]*Technische Universität Dresden, D-01069 Dresden, Germany*

(Received 28 March 2017; published 14 July 2017)

An extension of the atomic mass surface in the region $A \approx 100$ was performed via measurements of the $^{100-102}$Sr and $^{100-102}$Rb masses with the ion-trap spectrometer ISOLTRAP at CERN-ISOLDE, including the first direct mass determination of ^{102}Sr and ^{101,102}Rb. These measurements confirm the continuation of the region of deformation with the increase of neutron number, at least as far as $N = 65$. To interpret the deformation in the strontium isotopic chain and to determine whether an onset of deformation is present in heavier krypton isotopes, a comparison is made between the experimental values and mean-field and beyond mean-field results available in the literature. To complete this comparison Hartree-Fock-Bogoliubov calculations for even and odd isotopes were performed, illustrating the competition of nuclear shapes in the region.

DOI: 10.1103/PhysRevC.96.014310

I. INTRODUCTION

Nuclear structure rarely comes close to the simple scheme of independent nucleons occupying a set of single-particle levels generated by a spherical mean field. Although this intuition works well for describing the qualitative properties of isotopes along or close to the so-called magic numbers, adding or removing only a few protons or neutrons makes the spherical shells break down because of the strong nucleon-nucleon correlations. From this context emerges the concept of nuclear deformation, as one regains part of the independent-particle intuition by allowing the mean field to deform by the phenomenon of spontaneous symmetry breaking [1].

One of the very important regions of nuclear deformation is located on the nuclear chart around mass number $A = 100$, between the isotopic chains of krypton ($Z = 36$) and molybdenum ($Z = 42$). This region is particularly interesting because of the sudden onset of deformation at $N = 60$ making it one of the most dramatic shape changes on the nuclear chart. A first experimental hint of the deformation of these nuclides was given in the work of Johansson in 1965, from spectroscopic studies of spontaneous fission fragments [2]. Since this discovery, considerable efforts have been made, both experimentally and theoretically, to understand the properties of the nuclides in the region [3–8].

Several β-decay studies have provided the identification of the lowest levels of rotational bands. These observations concerned mostly the even-even nuclei [9–14]. The drop of the energy of the first 2^+ excited state at $N = 60$ in the strontium ($Z = 38$), zirconium ($Z = 40$), and molybdenum ($Z = 42$) isotopic chains was also regarded as a clear indication of their deformation [15].

Ground-state properties are also very good indicators of nuclear deformation. To highlight these properties the region of interest was extensively studied by laser spectroscopy. The mean-square charge radii determined from isotope-shift measurements were found to show a sudden increase at $N = 60$ [16–21].

Mass measurements already probe a large part of the region, allowing the determination of binding-energy differences, such as the two-neutron separation energy S_{2n}; see Sec. IV for details. Again, the sudden increase at $N = 60$ is a signature of nuclear deformation [22–24].

The knowledge of two-neutron separation energies generally extends further than other observables in the region, thus

*antoine.a.deroubin@jyu.fi; Present address: Department of Physics, University of Jyväskylä, P.O. Box 35 (YFL), FIN-40014, Finland.

†Present address: Technische Universität Dresden, 01069 Dresden, Germany.

‡Hochschule Mannheim, Paul-Wittsack-Str. 10, 68163 Mannheim.

§Present address: CERN, 1211 Geneva, Switzerland.

‖Present address: Institut de Physique Nuclaire, 15 Rue Georges Clemenceau, 91406 Orsay, France.

¶Present address: RIKEN Nishina Center, 2-1 Hirosawa, Wako-shi, Saitama 351-0198, Japan.

**Present address: ARC Center of Excellence for Engineered Quantum Systems, School of Physics, The University of Sydney, NSW 2006, Australia.

offering the first hints of possible structure changes. The majority of data originate from Penning-trap mass measurements [25,26]. The high-precision two-neutron separation energies show that nuclear structure does not change significantly with neutron number, once deformation sets in at $N = 60$. However, this statement might not be valid for higher neutron numbers. To find a limit to the region of deformation further mass measurements are needed.

Most recent results addressed the low-Z border of the deformation region [23,24,27,28]. They show that the nuclear structure changes with decreasing proton number. Indeed, ^{96}Kr and ^{97}Kr no longer exhibit the increase in S_{2n}, highlighting krypton as the boundary of the shape-transition region [27]. This conclusion is in agreement with charge-radii data [16] and is confirmed by Coulomb-excitation measurement of the first excited 2^+ state of ^{96}Kr [29]. However, it still remains unclear if the onset of deformation is completely absent in the krypton isotopic chain, or simply shifted to a higher neutron number.

The masses of $^{100-102}$Sr and $^{100-102}$Rb presented in this work were measured in 2014 with the precision Penning trap [30] and the multireflection time-of-flight mass spectrometer (MR-ToF MS) [31], respectively, of ISOLTRAP at ISOLDE/CERN [32]. The following section of this article is dedicated to the description of the ISOLTRAP setup. The results will be detailed in the third section, including the presentation of the first high-precision mass measurement of ^{102}Sr, ^{101}Rb, and ^{102}Rb.

A widely used approach for the description of $A \approx 100$ nuclei is the self-consistent mean-field Hartree-Fock-Bogoliubov (HFB) approximation. Two different types of effective nucleon-nucleon interactions are commonly used, namely Skyrme (with various parametrizations, such as SLy4 [33], UNEDF0 [34], and UNEDF1 [35]) and Gogny (with the Gogny D1S [36,37] parametrization and beyond-mean-field extensions in a five-dimensional collective Hamiltonian formalism (5DCH) [38,39]). The systematics of the two-neutron separation energies as well as charge radii calculated with these effective interactions will be presented. A comparison between the experimental and theoretical data will be discussed in the fourth section of the article.

II. EXPERIMENTAL SETUP

The rubidium and strontium isotopes were provided by the ISOLDE radioactive ion beam facility at CERN [32]. A proton beam of 1.4 GeV was sent on a thick uranium carbide target, creating fission products. Thermal effusion and diffusion processes allowed one to extract the neutral fission products from the hot target (ca. 2000°C). They were then surface ionized in a heated tantalum cavity (ca. 1800°C−2000°C). The resulting singly charged ions were accelerated to 30 keV, mass selected by the ISOLDE high-resolution separator (HRS), and transported to the ISOLTRAP setup.

The ISOLTRAP mass spectrometer [30,40], shown schematically in Fig. 1, consists of four ion traps: a radio-frequency quadrupole (RFQ) cooler and buncher [41], the MR-ToF MS [31], and two Penning traps, a cylindrical one, for ion bunch preparation [42], and a hyperbolic one for precision

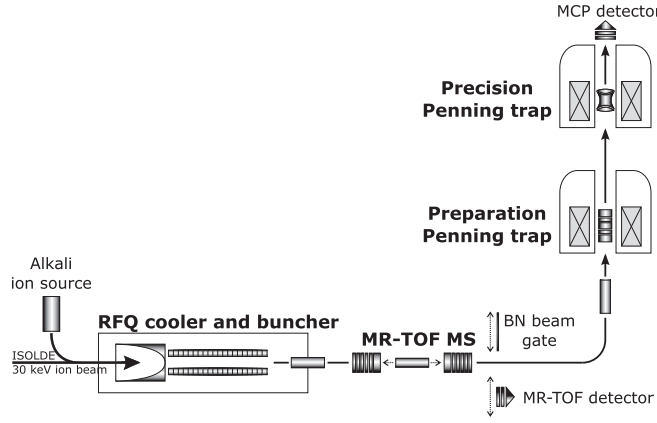

FIG. 1. Scheme of the ISOLTRAP mass spectrometer. For details, see text.

mass spectrometry. An ion mass can be determined either with the MR-ToF MS, or with the precision Penning trap.

The incoming quasicontinuous ion beam is first accumulated in the RFQ and then delivered as an ion bunch to the MR-ToF MS in which the ion bunch has a kinetic energy of ∼2.1 keV and a width between 100 and 200 ns. A more detailed discussion about the ion-bunch characteristics of the MR-ToF MS can be found in [31]. Inside the MR-ToF MS the ions undergo multiple reflections until an isobaric mass separation is reached [43]. This mass separation is expressed by a time-of-flight (ToF) difference between the different ion species, which is determined with a detector located behind the MR-ToF MS, giving access to the respective masses. The total time of flight is connected to the mass-over-charge ratio by the relation:

$$t = a\sqrt{\frac{m}{q}} + b, \tag{1}$$

where a and b are device-specific parameters. Their determination involves the time-of-flight measurement of two reference ions. One of the reference ions is an isobaric component of the on-line spectrum. An example of mass separation after 1000 revolutions is shown in Fig. 2 with ^{101}Rb$^+$ being the ion of interest and ^{101}Sr$^+$ the isobaric reference ion. The second reference ion is provided by the off-line alkali-metal ion source. The off-line data are taken with the same conditions as the on-line spectrum, i.e., same preparation by the RFQ and same number of ion revolutions inside the MR-ToF MS. The three measured time-of-flight values give access to the mass m of the ion of interest via the parameter C_{tof}, calculated from Eq. (1).

$$C_{\mathrm{tof}} = \frac{t}{t_{\mathrm{ref},1} - t_{\mathrm{ref},2}} - \frac{t_{\mathrm{ref},1} + t_{\mathrm{ref},2}}{2(t_{\mathrm{ref},1} - t_{\mathrm{ref},2})}, \tag{2}$$

and

$$\sqrt{m} = C_{\mathrm{tof}} \times (\sqrt{m_{\mathrm{ref},1}} - \sqrt{m_{\mathrm{ref},2}}) + \frac{1}{2} \times (\sqrt{m_{\mathrm{ref},1}} + \sqrt{m_{\mathrm{ref},2}}), \tag{3}$$

TABLE I. Half-lives [49] and frequency ratios of $^{100,101,102}Sr^{+}$, relative to $^{85}Rb^{+}$ ($ME(^{85}Rb) = -82167.330(5)$ keV/c^2 [22]), measured with ISOLTRAP's precision Penning trap. The corresponding mass excess values (ME_{ISOLTRAP}) and values from AME2012 [22] (ME_{AME2012}) are given, as well as $\Delta_{\text{ISOLTRAP-AME2012}}$. In the last column are shown the results of a recent publication (2016) from the TITAN experiment [24], not yet included in the AME2012.

Isotope	Half-life (ms)	$r = \nu_{c,\text{ref}}/\nu_c$	ME_{ISOLTRAP} (keV/c^2)	ME_{AME2012} (keV/c^2)	$\Delta_{\text{ISOLTRAP-AME2012}}$ (keV/c^2)	ME_{TITAN} (keV/c^2)
^{100}Sr	202(3)	1.176937584(344)	–59821(27)	–59830(10)	9(29)	–59816(11)
^{101}Sr	113.8(1.7)	1.188771552(259)	–55315(21)	–55560(80)	245(83)	–55327.6(9.8)
^{102}Sr	69(6)	1.200588455(846)	–52160(67)	–52360(70)	200(97)	

with $m_{\text{ref},i}$ and $t_{\text{ref},i}$ the mass and the time of flight of the reference ion i, respectively [44].

When a Penning-trap measurement is performed, the MR-ToF MS is used as a beam purifier. Instead of the time-of-flight detector, a Bradbury-Nielsen gate (BNG) is used to remove all unwanted ions from the beam [43]. The ions of interest are in this case transported to the first Penning trap for another step of cooling and purification, and then to the precision Penning trap for the measurement of the cyclotron frequency, from which the ion's mass m can be determined by use of the well-known relation,

$$m = \frac{1}{2\pi}\frac{qB}{\nu_c}, \tag{4}$$

where q is the ion's charge, B is the magnetic field strength, which is calibrated via the measurement of the cyclotron frequency of a reference ion of well-known mass (in this example $^{85}Rb^{+}$), and m the mass of the ion of interest. The frequencies ν_c were measured by the time-of-flight ion cyclotron resonance (ToF-ICR) method [45]. In the present experiment the Ramsey-type ToF-ICR method [46,47] was also used (an example is shown in Fig. 3). These two techniques are based on applying excitation signals on the precision trap electrodes which allow one to control the radial motion amplitude of the ions. Indeed, once trapped an ion has two radial eigenmotions, the magnetron and the modified cyclotron motions, with the corresponding eigenfrequencies ν_- and ν_+, respectively. Moreover, the addition of these two eigenfrequencies is equal to the ion's cyclotron frequency ν_c. By applying first a phase-locked dipole excitation [48] at the magnetron frequency one can increase the magnetron motion amplitude. A quadrupole excitation at the cyclotron frequency follows, allowing one to convert the magnetron motion into modified cyclotron motion periodically and thus modifying the radial energy of the ion. When the excitation frequency is equal to ν_c there is a full conversion of the magnetron to modified cyclotron motion and the ion's radial energy is maximized. This gain in radial energy can be measured via the decrease of the ion's time of flight from the trap to the detector [30]. The mass of the neutral atom of interest M, determined relatively to the well-known mass of a reference ion M_{ref} can be calculated via

$$M = r(M_{\text{ref}} - M_e) + M_e, \tag{5}$$

where M_{ref} is the mass of the reference ion and M_e the electron mass; the electron binding energy is neglected. $r = \nu_{c,\text{ref}}/\nu_c$ is the cyclotron-frequency ratio between the reference ion ($\nu_{c,\text{ref}}$) and the ion of interest (ν_c).

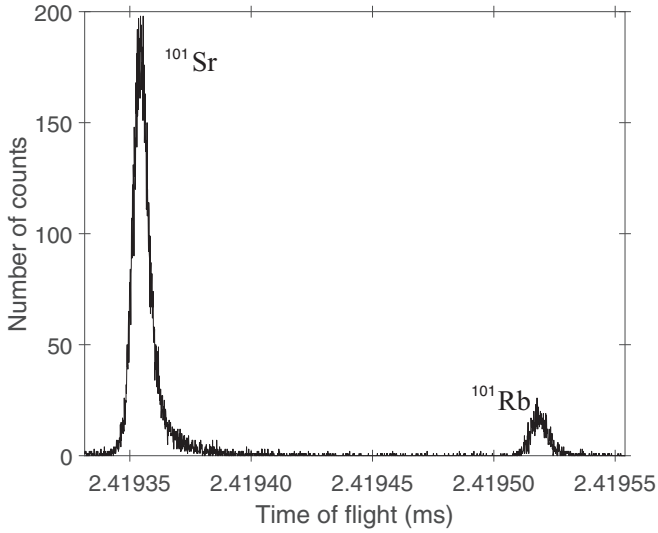

FIG. 2. Time-of-flight spectrum of ^{101}Sr and ^{101}Rb ions after 1000 revolutions inside the MR-ToF MS.

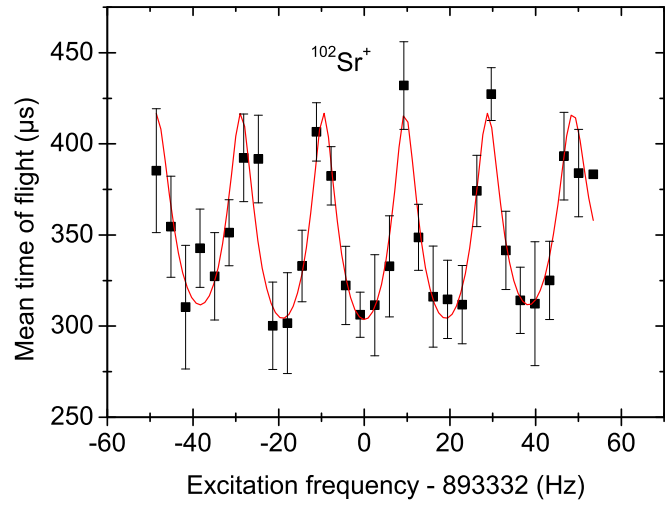

FIG. 3. Ramsey-type time-of-flight ion cyclotron resonance of ^{102}Sr ions with the fit curve for determining the cyclotron frequency [46].

TABLE II. Half-lives [49] and C_{tof} values of $^{100,101,102}Rb^+$ measured with the MR-ToF MS. The corresponding on-line reference is shown in brackets; the off-line reference is always $^{85}Rb^+$ ($ME(^{85}Rb) = -82167.330(0.005)$ keV/c^2 [22]). The corresponding mass excess ($ME_{ISOLTRAP}$) values are presented. Two mass excess values not yet included in the AME2012 are also shown, one obtained from a previous mass measurement performed at ISOLTRAP in 2013 ($ME_{ISOLTRAP\ 2013}$) [23], and from the TITAN experiment (ME_{TITAN}) [24].

Isotope (On-line ref.)	Half-life (ms)	C_{tof}	$ME_{ISOLTRAP}$ (keV/c^2)	$ME_{ISOLTRAP\ 2013}$ (keV/c^2)	ME_{TITAN} (keV/c^2)
^{100}Rb (^{100}Sr)	48(3)	0.50092961(111)	–46290(19)	–46247(20)	–46190(140)
^{101}Rb (^{101}Sr)	31.8(3.3)	0.50081901(123)	–42558(28)		
^{102}Rb (^{102}Sr)	37(3)	0.50089852(295)	–37253(83)		

III. RESULTS

The masses of $^{100-102}$Sr were measured with the precision trap, and the masses of $^{100-102}$Rb with the MR-ToF MS. In the MR-ToF MS spectra, both rubidium and its strontium isobar were present. As the ^{101,102}Sr masses were precisely determined in this work, they could be used in the ^{101,102}Rb mass determination process. For the ^{100}Rb mass determination, the well-known ^{100}Sr mass value referred to in the AME2012 [22] was used.

The experimental results are summarized in Table I (Penning-trap measurements) and Table II (MR-ToF MS measurements) as mass-excess values, the difference between the mass and the nuclide's mass number times the atomic mass unit: $ME(N,Z) = M(N,Z) - A \times u$. The existing literature values are also presented when available.

A. ^{100}Sr and ^{100}Rb

The ^{100}Sr mass was determined via a ToF-ICR resonance of 200 ms excitation time, the resulting mass excess being $ME_{ISOLTRAP} = -59821(27)$ keV/c^2 (Table I). The result is in agreement with two other Penning-trap mass measurements, one performed at JYFLTRAP [25] (the corresponding mass excess is $ME_{JYFLTRAP} = -59828(10)$ keV/c^2; it is the dominant contribution to the AME2012 mass table [22]) and one performed more recently at TITAN ($ME_{TITAN} = -59816(11)$ keV/c^2) [24].

In 2013 a mass measurement of ^{100}Rb was already reported in [23]. It was performed with the precision trap of the ISOLTRAP mass spectrometer; the mass excess value determined is $ME_{ISOLTRAP\ 2013} = -46247(20)$ keV/c^2. In the present work the ^{100}Rb mass was also measured, however, because of losses in the transport from the MR-ToF MS to the precision Penning trap, the ^{100}Rb mass could only be measured with the MR-ToF MS.

For the $^{100}Rb^+$ MR-ToF MS mass measurement the $^{100}Sr^+$ ions were used as an on-line reference (the mass excess value of ^{100}Sr referred in the AME2012, $ME(^{100}Sr) = -59830(10)$ keV/c^2 [22], was used to compute the ^{100}Rb mass excess), while for the off-line reference $^{85}Rb^+$ ions were used. Six time-of-flight spectra were taken. For five of them, the ions underwent 500 revolutions in the MR-ToF MS, for the last spectra the number of revolutions was 1000. The evaluated ^{100}Rb mass excess is $ME_{ISOLTRAP} = -46290(19)$ keV/c^2. It agrees within one and a half standard deviations with the previous ISOLTRAP measurement performed in 2013 with the precision Penning trap result [23]: $\Delta_{ISOLTRAP\text{-}ISOLTRAP\ 2013} = 43(26)$ keV/c^2, and within one standard deviation with the recent Penning-trap measurement from TITAN [24]: $\Delta_{ISOLTRAP\text{-}TITAN} = 100(141)$ keV/c^2.

B. ^{101}Sr and ^{101}Rb

Two conventional ToF-ICR measurements with 100 ms excitation time and two Ramsey-type measurements with two 10 ms excitation periods and 80 ms waiting time in between were made with the precision trap for ^{101}Sr. Our mass excess of $ME_{ISOLTRAP} = -55315(21)$ keV/c^2 deviates by 3σ from the AME2012 value [22] but agrees with the mass measurement performed recently at TITAN: $ME_{TITAN} = -55327.6(9.8)$ keV/c^2 [24].

We report here the first mass measurement of ^{101}Rb. Two time-of-flight spectra were taken with the MR-ToF MS, both with 1000 revolutions. A time-of-flight spectrum is shown in Fig. 2. The $^{85}Rb^+$ and the $^{101}Sr^+$ ions [$ME(^{101}Sr) = -55315(21)$ keV/c^2] were used for off-line and on-line references, respectively. The resulting mass excess is $ME_{ISOLTRAP} = -42558(28)$ keV/c^2.

C. ^{102}Sr and ^{102}Rb

We are presenting the first direct ion-trap mass measurements of ^{102}Sr and ^{102}Rb. The ^{102}Sr mass was determined via a single-excitation-pulse ToF-ICR measurement of 80 ms excitation time, and a Ramsey-type measurement of two 10 ms excitation periods and 40 ms waiting time in between. The Ramsey resonance is shown in Fig. 3. The corresponding mass excess is $ME_{ISOLTRAP} = -52160(67)$ keV/c^2. The AME2012 value of ^{102}Sr is a result of a β-endpoint measurement for ^{102}Sr (β^-) ^{102}Y.

Concerning ^{102}Rb, six time-of-flight spectra were taken, two with 500 revolutions and four with 1000 revolutions. The $^{85}Rb^+$ and the $^{102}Sr^+$ ions [$ME(^{102}Sr) = -52160(67)$ keV/c^2] were used for off-line and on-line references, respectively. The resulting mass excess is $ME_{ISOLTRAP} = -37253(83)$ keV/c^2.

IV. DISCUSSION

Figure 4(a) shows the evolution of the mass surface along the Sr, Rb, and Kr isotopic chains via the S_{2n} values in the region of nuclides of $A \approx 100$ [22]. The S_{2n} is the binding energy difference between two isotopes having N and $N-2$ neutron number, respectively: $S_{2n} = -M(A,Z)c^2 + M(A-2,Z)c^2 + 2M_nc^2$, where M_n is the neutron mass. In Fig. 4(b)

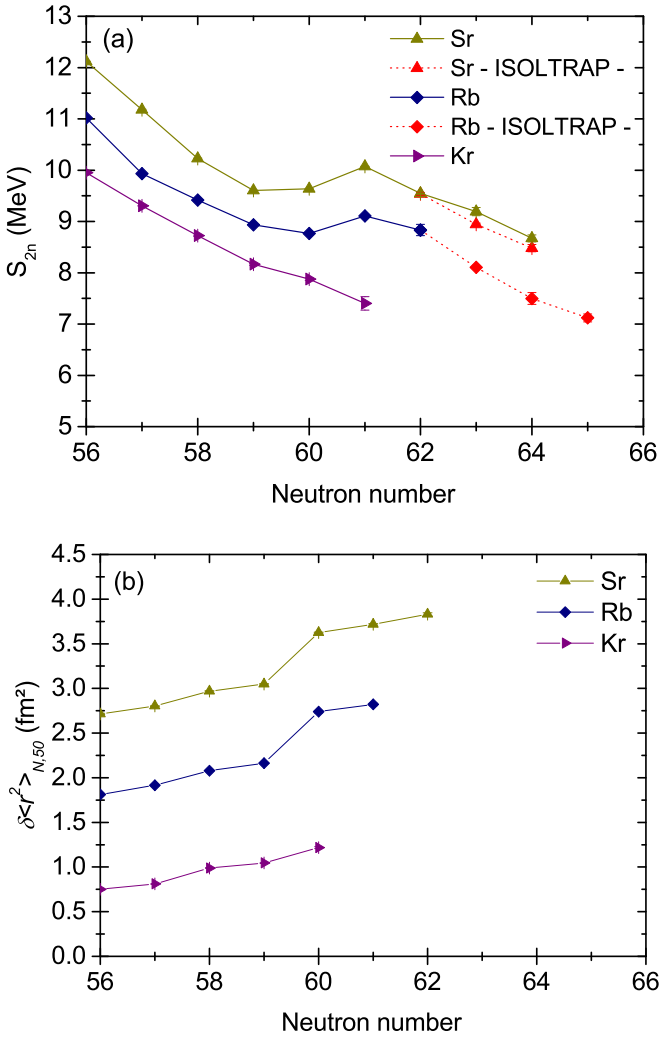

FIG. 4. (a) Experimental two-neutron separation energies in the $A \approx 100$ region. The experimental values from the AME2012 [22] are shown with solid points in different colors, the newly reported values of strontium and rubidium are shown with red solid points and dotted lines. (b) Evolution of experimental mean-square charge radii $\delta\langle r^2\rangle_{N,50}$, relative to the corresponding $N = 50$ isotopes, in the same region [16–19]. To avoid an overlap of the $\delta\langle r^2\rangle_{N,50}$ curves, they are plotted with an arbitrary offset with respect to the krypton chain.

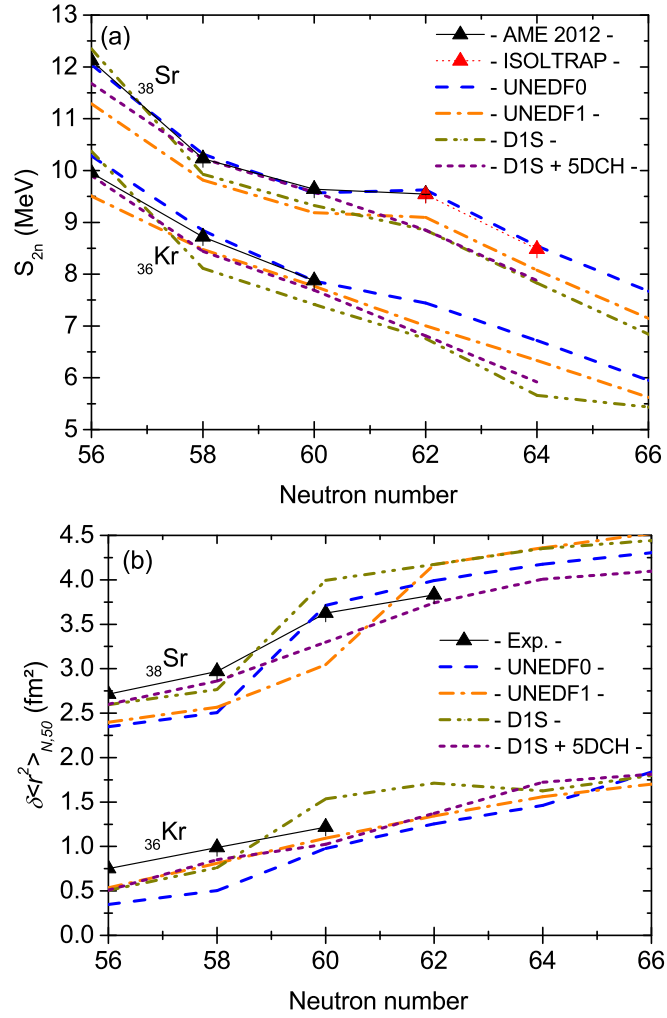

FIG. 5. Experimental two-neutron separation energies (a), and mean-square charge radii (b), for the strontium and krypton isotopic chains. The data are compared to three self-consistent HFB calculations and a beyond-mean-field calculation. For details see text. To avoid an overlap of the $\delta\langle r^2\rangle_{N,50}$ curves, the Sr isotopic chains are plotted with an arbitrary offset of 2 fm^2 with respect to the krypton chain.

are plotted the mean-square charge radii ($\delta\langle r^2\rangle_{N,50}$) in the same region, represented as differences to the isotope with $N = 50$ [16–19].

In Fig. 4(a), the increase of S_{2n} at $N = 60$ for the Sr and Rb isotopic chains signals the sudden onset of collectivity in the ground state. The new S_{2n} values of the Sr and Rb isotopes show that the deformation which appears at $N = 60$ remains at least as far as $N = 64$ and $N = 65$, respectively, without major structural changes. This conclusion is also supported by the recent identification of the level scheme in ^{102}Sr [50]. The shape transitions and the persistence of the ground-state deformations, up to $N = 62$, are visible also in the evolution of the mean-square charge radii, as shown in Fig. 4(b). We note that $N = 66$ is the midshell between the magic neutron numbers $N = 50$ and $N = 82$.

In Fig. 5 the even-even experimental S_{2n} and $\delta\langle r^2\rangle_{N,50}$ are compared to theoretical models. The calculations are available only for even-even nuclei, therefore, the rubidium isotopic chain is not shown. The models presented belong to a class of self-consistent mean-field approaches [51] with two different effective interactions between nucleons: Skyrme and Gogny. Two parametrizations of the Skyrme interaction are shown: UNEDF0 (adjusted on spherical and deformed nuclei) [34], and UNEDF1 (optimized also on the excitation energies of fission isomers) [35]. For the Gogny interaction, only the D1S parametrization is shown [36,37]. The Gogny D1S + 5DCH is a beyond mean-field calculation, which uses a five-dimensional collective Hamiltonian (5DCH) [38].

Of the Skyrme effective interactions, the parametrization which gives the best description is UNEDF0. One can see in Fig. 5 an excellent agreement between the experimental data

and the model in the strontium isotopic chain (especially for S_{2n}). Slightly worse agreement is found with the UNEDF1 model. Indeed, even if an onset of deformation and a similar trend can be noticed in the S_{2n} values of Sr, there is an offset of the calculated results from the experimental data.

The calculations with the Gogny effective interaction give a worse description of the onset of deformation. A sudden increase is predicted at $N = 60$ for the strontium charge radii, but not for the two-neutron separation energy. Furthermore, the introduction of the beyond mean-field calculations D1S+5DCH do not help to reproduce the onset of deformation.

The Skyrme density functional theory calculations predict that the shape transition taking place in the strontium isotopic chain is not existent (or at least much weaker) in the krypton isotopic chain. In the D1S mean-field calculation, a clear transition is predicted for ^{96}Kr $\delta\langle r^2\rangle_{N,50}$ (visible as a small increase of the ^{96}Kr charge radius). However, when the beyond mean-field calculation is included, this effect vanishes.

Whether the "southwest" border of the region of deformation is in the krypton or the rubidium isotopic chain is an open question. The masses of ^{96,97}Kr were precisely measured for the first time in 2010, see [27], and no sign of deformation was found. Therefore, ^{97}Rb was defined as the lightest deformed $N = 60$ isotone, which is also supported by the recent work of Coulomb excitation by Sotty *et al.* [52].

The state-of-the-art calculations presented so far allow discussing the overall trend of the ground-state properties along the isotopic chains of interest. However, to better understand this trend, it is worth also examining the evolution as a function of neutron number of the major intrinsic configurations in the region. Furthermore, the fact that odd nuclei are not computed limits the possibility of completely quantifying the strength of the increase in two-neutron separation energies across $N = 60$. To provide this missing information, HFB calculations were performed for the even- and odd-N Sr and Kr isotopic chains. The symmetry-unconstrained HFODD [53] code and the SLy4 interaction [33], with a contact volume-pairing force, were used. The HFODD solver uses the expansion of the wave function in a harmonic-oscillator (HO) basis. For this work a spherical basis of a maximum of 500 HO functions was used. The region of deformation was already studied with the HFODD solver and the SLy4 interaction in [23]. But there, the odd-A and the odd-odd nuclei were calculated in the so-called false vacuum interaction, meaning with fully paired wave functions [54]. As an extension to this work, here we computed the odd-A nuclei in the blocking approximation. This method, detailed in [55], allows a complete description of odd nuclei.

Because of its essential role in the Federman-Pittel mechanism [56], the pairing force had to be adjusted in the calculations to reproduce the nuclear deformation. Similarly to the works presented in [23] and [57], in the current work the pairing interaction was tuned on the odd-even staggering of the binding energies of Sn isotopes between $N = 67$ and $N = 73$, in a spherical calculation. An equal pairing interaction of -200 MeVfm^3 was chosen for protons and neutrons.

In the calculations, both oblate and prolate solutions were found lying close in energy, in agreement with the results presented in [58,59] for a Gogny-type interaction, and with the results presented in [23] for a Skyrme-type interaction.

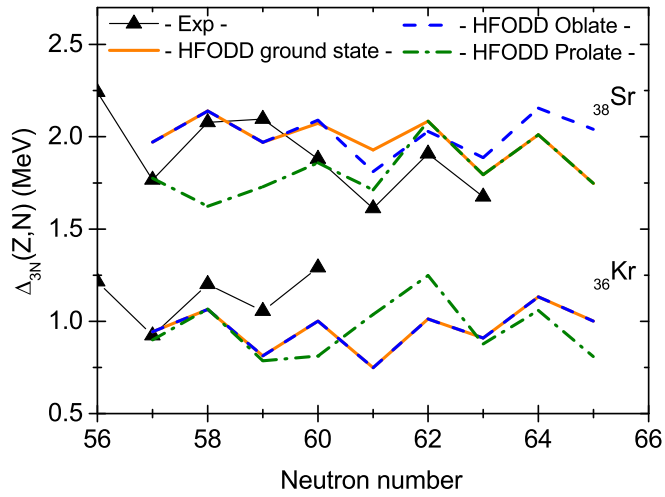

FIG. 6. Comparison of the experimental odd-even staggering in the region $A \approx 100$ with HFODD calculations. The experimental values from the AME2012 [22] are shown with black solid points and the calculated ground state, prolate-deformed and oblate-deformed solutions with line, dashed line, and dot-dashed line, respectively. To avoid an overlap between the curves, the Sr isotopic chains are plotted with an arbitrary offset of 1 MeV with respect to the Kr chains.

In Fig. 6 the odd-even staggering of the computed nuclides is represented via the three-point estimator:

$$\Delta_{3N}(Z,N) = \frac{(-1)^N}{2}(B(Z,N-1) - 2B(Z,N) + B(Z,N+1)), \quad (6)$$

where $B(Z,N)$ is the binding energy of the nucleus with Z protons and N neutrons (taken with negative sign). The good agreement between the experimental and computed odd-even staggering shows that the pairing force was properly set for these calculations. Furthermore, one notices in the experimental data that the onset of deformation is also reflected in the trend of Δ_{3N} by a flattening right before the onset of deformation of its oscillatory trend. This feature is described qualitatively by the prolate solution of the calculations in both the strontium and krypton isotopic chains.

In Fig. 7 the two-neutron separation energy and the mean-square charge radii resulting from the HFB calculations are compared to the available experimental data in the region $A \approx 100$.

Similarly to the HFODD calculations presented in [23], the prolate solution describes best the observed systematics of the two-neutron separation energy beyond $N = 60$. In general, two prolate configurations are found, depending on the neutron number range: one state at lower deformation for $N < 60$, and one at larger deformation emerging at $N \sim 60$. One way to explain the shape transition is thus a change around $N = 60$ from low-deformation to high-deformation prolate shape. Alternatively, the shape transition takes place as a change between an oblate and a prolate shape. The calculations, presented in Figs. 6 and 7, favor the latter situation, because the oblate configuration is predicted to be lower in energy for $N < 60$. However, if one simply assigns the ground state

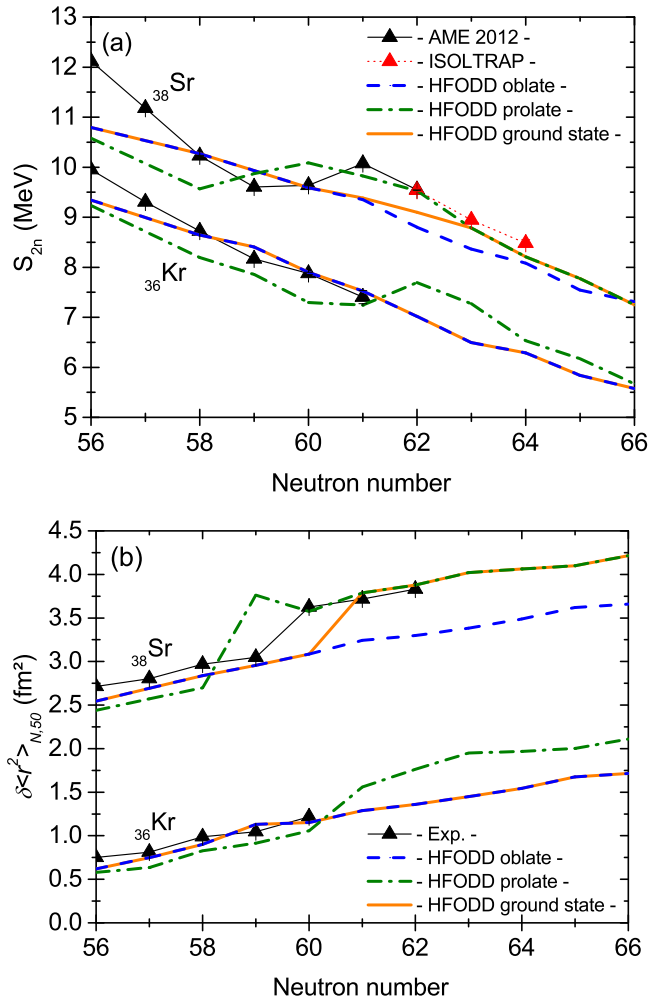

FIG. 7. Comparison of the experimental two-neutron separation energy (a) and mean-square charge radii (b) in the region $A \approx 100$ with HFODD calculations. The experimental values from the AME2012 [22] are shown with black solid triangles, the newly reported values of strontium and rubidium with a dotted line and red solid triangles, and the calculated ground state, prolate-deformed and oblate-deformed solutions with line, dashed line, and dot-dashed line, respectively. The odd nuclei are computed only between $N = 57$ and $N = 65$. To avoid an overlap of the $\delta\langle r^2\rangle_{N,50}$ curves, the Sr isotopic chains are plotted with an arbitrary offset of 2 fm^2 with respect to the Kr chains.

of each isotope to the configuration of lowest energy, the strength of the effect in S_{2n} at $N = 60$ is underestimated. This is because the change in binding energy which accompanies the oblate-prolate transition is not strong enough. One must note, however, that the spectroscopic quadrupole moments determined by laser spectroscopy [16–18] are positive for $N < 60$, indicating a prolate nature of the ground state. This could point to the fact that the ordering in energy between the two configurations is incorrectly predicted by the HFB calculations, or that beyond-mean-field configuration mixing is very important for the nuclei with $N < 60$. We note that the UNEDF0 and UNEDF1 calculations predict almost spherical shapes for strontium isotopes with $N < 60$ and oblate shapes for the corresponding krypton isotopes.

The krypton isotopes are not predicted to be in the region of strong deformation; see Figs. 6 and 7. A similar conclusion was found in [23,27]. Nevertheless, a transition between weakly deformed and strongly deformed shape is still predicted to take place in the prolate solution for higher neutron number: $N = 61,62$. Measurements of heavier krypton isotopes (^{98}Kr and further) are thus mandatory to clarify their shape evolution towards the neutron midshell ($N = 66$) and to establish whether the krypton chain is indeed the boundary of the prolate shape transition of the region of deformation [23,27].

The evolution of the intrinsic deformation of even-even krypton isotopes was studied in [60]. The so-called symmetry-conserving configuration-mixing (SCCM) method with the Gogny D1S interaction was used to explore the triaxial degree of freedom of the krypton isotopes beyond the mean field. It was found that at the mean-field level the triaxiality of ^{98}Kr is low and that beyond the mean field, the wave functions of the ground and first excited bands are dominated by the oblate and prolate configuration, respectively. This means that the fingerprints of the static intrinsic shapes of the krypton isotopes might be traceable at the level of the ground-state observables beyond $N = 60$.

V. CONCLUSION

We presented mass measurements of ^{100,101,102}Rb and ^{100,101,102}Sr performed at the ISOLDE/CERN facility with ISOLTRAP by using the MR-ToF MS, for the rubidium masses, and the precision Penning trap for the strontium masses. The isotopes ^{102}Sr, ^{101}Rb, and ^{102}Rb were investigated for the first time. The measured masses continue the trend in the region of deformation well beyond $N = 60$, approaching the nuclear midshell.

Different self-consistent mean-field approaches (including a beyond-mean-field approach) with different Skyrme and Gogny effective interactions were applied. The calculations with the different nucleon-nucleon interactions (namely Skyrme and Gogny) tend to reproduce the properties of the even-even nuclei in the region of interest. Furthermore, HFB calculations with the HFODD solver and the SLy4 Skyrme interaction were shown for the odd-N krypton and strontium isotopes. The prolate solution gives a good agreement with the experimental data, but the calculation predicts the oblate solution to be lower in energy for $N < 60$, which attenuates a lot the increase in S_{2n} at the shape transition point. Furthermore, these calculations exclude the krypton chain from the region of strong deformation, but a transition between weakly deformed and strongly deformed shape is still predicted to take place in the prolate solution for higher neutron number: $N = 61,62$.

The region of deformation has been an interesting topic for many years, and the recent results [50,52,60,61], including this work, confirm the continuity of the nuclear ground-state deformation beyond $N = 60$ in the isotopic chains of zirconium, yttrium, strontium, and rubidium. Up to now, no shape transition was observed in the isotopes of krypton. However, the recently published results from [60] predict shape coexistence in ^{98}Kr. The measurement of heavier krypton isotopes is the next step to highlight whether the "southwest" border of the deformation is ^{97}Rb or ^{98}Kr. The

determination of the border will allow to better constrain models dedicated to nuclear deformation.

ACKNOWLEDGMENTS

We thank the ISOLDE technical group and the ISOLDE Collaboration for their support. Stimulating discussions with S. Peru-Desenfants and P. Ascher are gratefully acknowledged. We acknowledge support from the BMBF (05P12HGCI1, 05P12HGFNE, 05P15HGCIA, and 05P15ODCIA), Nuclear Astrophysics Virtual Institute (NAVI) of the Helmholtz Association, Helmholtz-CAS Joint Research Group (HCJRG-108), the Max-Planck Society, the European Union 7th framework through ENSAR (Contract No. 262010), the French IN2P3, the Helmholtz Alliance Program, Contract No. HA216/EMMI, and the STFC under Grants No. ST/L005743/1 and No. ST/L005816/1. D.A. acknowledges support from the IMPRS-PTFS. S.K. acknowledges support from the Robert Bosch Foundation.

[1] P. Ring and P. Schuck, *The Nuclear Many-body Problem* (Springer Science & Business Media, Berlin/Heidelberg, 2004).
[2] S. A. Johansson, Nucl. Phys. **64**, 147 (1965).
[3] E. Cheifetz, R. C. Jared, S. G. Thompson, and J. B. Wilhelmy, Phys. Rev. Lett. **25**, 38 (1970).
[4] R. E. Azuma, G. L. Borchert, L. C. Carraz, P. G. Hansen, B. Jonson, S. Mattsson, O. B. Nielsen, G. Nyman, I. Ragnarsson, and H. L. Ravn, Phys. Lett. B **86**, 5 (1979).
[5] E. Kirchuk, P. Federman, and S. Pittel, Phys. Rev. C **47**, 567 (1993).
[6] M. A. C. Hotchkis, J. L. Durell, J. B. Fitzgerald, A. S. Mowbray, W. R. Phillips, I. Ahmad, M. P. Carpenter, R. V. F. Janssens, T. L. Khoo, E. F. Moore, L. R. Morss, P. Benet, and D. Ye, Nucl. Phys. A **530**, 111 (1991).
[7] J. Ebert, R. A. Meyer, and K. Sistemich, *Nuclear Structure of the Zirconium Region: Proceedings of the International Workshop* (Springer Science & Business Media, Berlin/Heidelberg, 2012).
[8] A. G. Smith, J. L. Durell, W. R. Phillips, W. Urban, P. Sarriguren, and I. Ahmad, Phys. Rev. C **86**, 014321 (2012).
[9] F. K. Wohn, J. C. Hill, R. F. Petry, H. Dejbakhsh, Z. Berant, and R. L. Gill, Phys. Rev. Lett. **51**, 873 (1983).
[10] F. K. Wohn, J. C. Hill, C. B. Howard, K. Sistemich, R. F. Petry, R. L. Gill, H. Mach, and A. Piotrowski, Phys. Rev. C **33**, 677 (1986).
[11] F. K. Wohn, J. C. Hill, J. A. Winger, R. F. Petry, J. D. Goulden, R. L. Gill, A. Piotrowski, and H. Mach, Phys. Rev. C **36**, 1118 (1987).
[12] R. F. Petry, J. D. Goulden, F. K. Wohn, J. C. Hill, R. L. Gill, and A. Piotrowski, Phys. Rev. C **37**, 2704 (1988).
[13] G. Lhersonneau, H. Gabelmann, N. Kaffrell, K. L. Kratz, B. Pfeiffer, and K. Heyde, Z. Phys. A **337**, 143 (1990).
[14] G. Lhersonneau, H. Gabelmann, B. Pfeiffer, and K. L. Kratz, Z. Phys. A **352**, 293 (1995).
[15] "Evaluated nuclear structure data file" [http://www.nndc.bnl.gov/ensdf/] (2016), last updated 06-24-2016.
[16] M. Keim, E. Arnold, W. Borchers, U. Georg, A. Klein, R. Neugart, L. Vermeeren, R. E. Silverans, and P. Lievens, Nucl. Phys. A **586**, 219 (1995).
[17] C. Thibault, F. Touchard, S. Büttgenbach, R. Klapisch, M. de Saint Simon, H. T. Duong, P. Jacquinot, P. Juncar, S. Liberman, P. Pillet, J. Pinard, J. L. Vialle, A. Pesnelle, and G. Huber, Phys. Rev. C **23**, 2720 (1981).
[18] F. Buchinger, E. B. Ramsay, E. Arnold, W. Neu, R. Neugart, K. Wendt, R. E. Silverans, P. Lievens, L. Vermeeren, D. Berdichevsky, R. Fleming, D. W. L. Sprung, and G. Ulm, Phys. Rev. C **41**, 2883 (1990).
[19] P. Lievens, R. E. Silverans, L. Vermeeren, W. Borchers, W. Neu, R. Neugart, K. Wendt, F. Buchinger, and E. Arnold, Phys. Lett. B **256**, 141 (1991).
[20] I. Angeli and K. P. Marinova, At. Data Nucl. Data Tables **99**, 69 (2013).
[21] T. J. Procter, J. A. Behr, J. Billowes, F. Buchinger, B. Cheal, J. E. Crawford, J. Dilling, A. B. Garnsworthy, A. Leary, C. D. P. Levy, E. Mané, M. R. Pearson, O. Shelbaya, M. Stolz, W. Al Tamimi, and A. Voss, Eur. Phys. J. A **51**, 23 (2015).
[22] M. Wang, G. Audi, A. H. Wapstra, F. G. Kondev, M. MacCormick, X. Xu, and B. Pfeiffer, Chin. Phys. C **36**, 1603 (2012).
[23] V. Manea, D. Atanasov, D. Beck, K. Blaum, C. Borgmann, R. B. Cakirli, T. Eronen, S. George, F. Herfurth, A. Herlert, M. Kowalska, S. Kreim, Y. A. Litvinov, D. Lunney, D. Neidherr, M. Rosenbusch, L. Schweikhard, F. Wienholtz, R. N. Wolf, and K. Zuber, Phys. Rev. C **88**, 054322 (2013).
[24] R. Klawitter, A. Bader, M. Brodeur, U. Chowdhury, A. Chaudhuri, J. Fallis, A. T. Gallant, A. Grossheim, A. A. Kwiatkowski, D. Lascar, K. G. Leach, A. Lennarz, T. D. Macdonald, J. Pearkes, S. Seeraji, M. C. Simon, V. V. Simon, B. E. Schultz, and J. Dilling, Phys. Rev. C **93**, 045807 (2016).
[25] U. Hager, T. Eronen, J. Hakala, A. Jokinen, V. S. Kolhinen, S. Kopecky, I. Moore, A. Nieminen, M. Oinonen, S. Rinta-Antila, J. Szerypo, and J. Äystö, Phys. Rev. Lett. **96**, 042504 (2006).
[26] A. Kankainen, J. Äystö, and A. Jokinen, J. Phys. G: Nucl. Part. Phys. **39**, 093101 (2012).
[27] S. Naimi, G. Audi, D. Beck, K. Blaum, C. Böhm, C. Borgmann, M. Breitenfeldt, S. George, F. Herfurth, A. Herlert, M. Kowalska, S. Kreim, D. Lunney, D. Neidherr, M. Rosenbusch, S. Schwarz, L. Schweikhard, and K. Zuber, Phys. Rev. Lett. **105**, 032502 (2010).
[28] V. V. Simon, T. Brunner, U. Chowdhury, B. Eberhardt, S. Ettenauer, A. T. Gallant, E. Mané, M. C. Simon, P. Delheij, M. R. Pearson, G. Audi, G. Gwinner, D. Lunney, H. Schatz, and J. Dilling, Phys. Rev. C **85**, 064308 (2012).
[29] M. Albers, N. Warr, K. Nomura, A. Blazhev, J. Jolie, D. Mücher, B. Bastin, C. Bauer, C. Bernards, L. Bettermann, V. Bildstein, J. Butterworth, M. Cappellazzo, J. Cederkäll, D. Cline, I. Darby, S. Das Gupta, J. M. Daugas, T. Davinson, H. De Witte, J. Diriken, D. Filipescu, E. Fiori, C. Fransen, L. P. Gaffney, G. Georgiev, R. Gernhäuser, M. Hackstein, S. Heinze, H. Hess, M. Huyse, D. Jenkins, J. Konki, M. Kowalczyk, T. Kröll, R. Krücken, J. Litzinger, R. Lutter, N. Marginean, C. Mihai, K. Moschner, P. Napiorkowski, B. S. Nara Singh, K. Nowak, T. Otsuka, J. Pakarinen, M. Pfeiffer, D. Radeck, P. Reiter, S. Rigby, L. M.

Robledo, R. Rodríguez-Guzmán, M. Rudigier, P. Sarriguren, M. Scheck, M. Seidlitz, B. Siebeck, G. Simpson, P. Thöle, T. Thomas, J. Van de Walle, P. Van Duppen, M. Vermeulen, D. Voulot, R. Wadsworth, F. Wenander, K. Wimmer, K. O. Zell, and M. Zielinska, Phys. Rev. Lett. **108**, 062701 (2012).

[30] M. Mukherjee, D. Beck, K. Blaum, G. Bollen, J. Dilling, S. George, F. Herfurth, A. Herlert, A. Kellerbauer, H. J. Kluge, S. Schwarz, L. Schweikhard, and C. Yazidjian, Eur. Phys. J. A **35**, 1 (2008).

[31] R. N. Wolf, F. Wienholtz, D. Atanasov, D. Beck, K. Blaum, C. Borgmann, F. Herfurth, M. Kowalska, S. Kreim, Y. A. Litvinov, D. Lunney, V. Manea, D. Neidherr, M. Rosenbusch, L. Schweikhard, J. Stanja, and K. Zuber, Int. J. Mass Spectrom. **349-350**, 123 (2013).

[32] E. Kugler, Hyperfine Interact. **129**, 23 (2000).

[33] E. Chabanat, P. Bonche, P. Haensel, J. Meyer, and R. Schaeffer, Nucl. Phys. A **635**, 231 (1998).

[34] M. Kortelainen, T. Lesinski, J. Moré, W. Nazarewicz, J. Sarich, N. Schunck, M. V. Stoitsov, and S. Wild, Phys. Rev. C **82**, 024313 (2010).

[35] M. Kortelainen, J. McDonnell, W. Nazarewicz, P.-G. Reinhard, J. Sarich, N. Schunck, M. V. Stoitsov, and S. M. Wild, Phys. Rev. C **85**, 024304 (2012).

[36] J. Dechargé and D. Gogny, Phys. Rev. C **21**, 1568 (1980).

[37] J. Berger, M. Girod, and D. Gogny, Comput. Phys. Commun. **63**, 365 (1991).

[38] G. F. Bertsch, M. Girod, S. Hilaire, J.-P. Delaroche, H. Goutte, and S. Péru, Phys. Rev. Lett. **99**, 032502 (2007).

[39] J.-P. Delaroche, M. Girod, J. Libert, H. Goutte, S. Hilaire, S. Péru, N. Pillet, and G. F. Bertsch, Phys. Rev. C **81**, 014303 (2010).

[40] S. Kreim, D. Atanasov, D. Beck, K. Blaum, C. Böhm, C. Borgmann, M. Breitenfeldt, T. E. Cocolios, D. Fink, S. George, A. Herlert, A. Kellerbauer, U. Köster, M. Kowalska, D. Lunney, V. Manea, E. M. Ramirez, S. Naimi, D. Neidherr, T. Nicol, R. E. Rossel, M. Rosenbusch, L. Schweikhard, J. Stanja, F. Wienholtz, R. N. Wolf, and K. Zuber, Nucl. Instrum. Methods Phys. Res. B **317**, 492 (2013).

[41] F. Herfurth, J. Dilling, A. Kellerbauer, G. Bollen, S. Henry, H.-J. Kluge, E. Lamour, D. Lunney, R. B. Moore, C. Scheidenberger, S. Schwarz, G. Sikler, and J. Szerypo, Nucl. Instrum. Methods Phys. Res. A **469**, 254 (2001).

[42] G. Savard, S. Becker, G. Bollen, H.-J. Kluge, R. B. Moore, T. Otto, L. Schweikhard, H. Stolzenberg, and U. Wiess, Phys. Lett. A **158**, 247 (1991).

[43] R. N. Wolf, D. Beck, K. Blaum, C. Böhm, C. Borgmann, M. Breitenfeldt, F. Herfurth, A. Herlert, M. Kowalska, S. Kreim, D. Lunney, S. Naimi, D. Neidherr, M. Rosenbusch, L. Schweikhard, J. Stanja, F. Wienholtz, and K. Zuber, Nucl. Instrum. Methods Phys. Res. A **686**, 82 (2012).

[44] F. Wienholtz, D. Beck, K. Blaum, C. Borgmann, M. Breitenfeldt, R. B. Cakirli, S. George, F. Herfurth, J. Holt, M. Kowalska, S. Kreim, D. Lunney, V. Manea, J. Menendez, D. Neidherr, M. Rosenbusch, L. Schweikhard, A. Schwenk, J. Simonis, J. Stanja, R. N. Wolf, and K. Zuber, Nature (London) **498**, 346 (2013).

[45] G. Gräff, H. Kalinowsky, and J. Traut, Z. Phys. A **297**, 35 (1980).

[46] M. Kretzschmar, AIP Conf. Proc. **457**, 242 (1999).

[47] S. George, S. Baruah, B. Blank, K. Blaum, M. Breitenfeldt, U. Hager, F. Herfurth, A. Herlert, A. Kellerbauer, H.-J. Kluge, M. Kretzschmar, D. Lunney, R. Savreux, S. Schwarz, L. Schweikhard, and C. Yazidjian, Phys. Rev. Lett. **98**, 162501 (2007).

[48] K. Blaum, G. Bollen, F. Herfurth, A. Kellerbauer, H.-J. Kluge, M. Kuckein, S. Heinz, P. Schmidt, and L. Schweikhard, J. Phys. B **36**, 921 (2003).

[49] G. Audi, F. G. Kondev, M. Wang, B. Pfeiffer, X. Sun, J. Blachot, and M. MacCormick, Chin. Phys. C **36**, 1157 (2012).

[50] Z. M. Wang, A. B. Garnsworthy, C. Andreoiu, G. C. Ball, P. C. Bender, V. Bildstein, D. S. Cross, G. Demand, R. Dunlop, L. J. Evitts, P. E. Garrett, G. Hackman, B. Hadinia, S. Ketelhut, R. Krücken, K. G. Leach, A. T. Laffoley, D. Miller, M. Moukaddam, J. Pore, A. J. Radich, M. M. Rajabali, C. E. Svensson, A. Tan, E. Tardiff, C. Unsworth, A. Voss, and P. Voss, Phys. Rev. C **93**, 054301 (2016).

[51] M. Bender, P.-H. Heenen, and P.-G. Reinhard, Rev. Mod. Phys. **75**, 121 (2003).

[52] C. Sotty, M. Zielińska, G. Georgiev, D. L. Balabanski, A. E. Stuchbery, A. Blazhev, N. Bree, R. Chevrier, S. Das Gupta, J. M. Daugas, T. Davinson, H. De Witte, J. Diriken, L. P. Gaffney, K. Geibel, K. Hadyńska-Klęk, F. G. Kondev, J. Konki, T. Kröll, P. Morel, P. Napiorkowski, J. Pakarinen, P. Reiter, M. Scheck, M. Seidlitz, B. Siebeck, G. Simpson, H. Törnqvist, N. Warr, and F. Wenander, Phys. Rev. Lett. **115**, 172501 (2015).

[53] N. Schunck, J. Dobaczewski, J. McDonnell, W. Satuła, J. A. Sheikh, A. Staszczak, M. Stoitsov, and P. Toivanen, Comput. Phys. Commun. **183**, 166 (2012).

[54] T. Duguet, P. Bonche, P.-H. Heenen, and J. Meyer, Phys. Rev. C **65**, 014310 (2001).

[55] J. Dobaczewski, W. Satuła, B. G. Carlsson, J. Engel, P. Olbratowski, P. Powałowski, M. Sadziak, J. Sarich, N. Schunck, A. Staszczak, M. Stoitsov, M. Zalewski, and H. Zduńczuk, Comput. Phys. Commun. **180**, 2361 (2009).

[56] P. Federman and S. Pittel, Phys. Rev. C **20**, 820 (1979).

[57] V. Manea, P. Ascher, D. Atanasov, A. E. Barzakh, D. Beck, K. Blaum, C. Borgmann, M. Breitenfeldt, R. B. Cakirli, T. E. Cocolios, T. Day Goodacre, D. V. Fedorov, V. N. Fedosseev, S. George, F. Herfurth, M. Kowalska, S. Kreim, Y. A. Litvinov, D. Lunney, B. Marsh, D. Neidherr, M. Rosenbusch, R. E. Rossel, S. Rothe, L. Schweikhard, F. Wienholtz, R. N. Wolf, and K. Zuber, Phys. Rev. C **95**, 054322 (2017).

[58] R. Rodríguez-Guzmán, P. Sarriguren, L. M. Robledo, and S. Perez-Martin, Phys. Lett. B **691**, 202 (2010).

[59] R. Rodríguez-Guzmán, P. Sarriguren, and L. M. Robledo, Phys. Rev. C **82**, 061302 (2010).

[60] T. R. Rodríguez, Phys. Rev. C **90**, 034306 (2014).

[61] E. Clément, M. Zielińska, A. Görgen, W. Korten, S. Péru, J. Libert, H. Goutte, S. Hilaire, B. Bastin, C. Bauer, A. Blazhev, N. Bree, B. Bruyneel, P. A. Butler, J. Butterworth, P. Delahaye, A. Dijon, D. T. Doherty, A. Ekström, C. Fitzpatrick, C. Fransen, G. Georgiev, R. Gernhäuser, H. Hess, J. Iwanicki, D. G. Jenkins, A. C. Larsen, J. Ljungvall, R. Lutter, P. Marley, K. Moschner, P. J. Napiorkowski, J. Pakarinen, A. Petts, P. Reiter, T. Renstrøm, M. Seidlitz, B. Siebeck, S. Siem, C. Sotty, J. Srebrny, I. Stefanescu, G. M. Tveten, J. Van de Walle, M. Vermeulen, D. Voulot, N. Warr, F. Wenander, A. Wiens, H. De Witte, and K. Wrzosek-Lipska, Phys. Rev. Lett. **116**, 022701 (2016).